RSC Advances

Magnetic and magnetocaloric properties of iron substituted holmium chromite and dysprosium chromite

Shiqi Yin,[a] Vinit Sharma,[b] Austin McDannald,[c] Fernando A. Reboredo,[b] and Menka Jain [a,d,*]

[a]Department of Physics, University of Connecticut, Storrs, CT 06269
[b]Materials Theory Group, Materials Science & Technology Division, Oak Ridge National Laboratory, Oak Ridge, TN 37831
[c]Materials Science and Engineering Department, University of Connecticut, Storrs, CT 06269
[d]Institute of Material Science, University of Connecticut, Storrs, CT 06269

Abstract

In this work, $HoCrO_3$ and Fe substituted $HoCrO_3$ and $DyCrO_3$ (*i.e.* $HoCr_{0.7}Fe_{0.3}O_3$ and $DyCr_{0.7}Fe_{0.3}O_3$) powder samples were synthesized via a solution route. The structural properties of the samples were examined by Raman spectroscopy and x-ray diffraction techniques, which were further confirmed using first-principle calculations. The dc magnetic measurements indicate that the Cr^{3+} ordering temperatures for the $HoCrO_3$, $HoCr_{0.7}Fe_{0.3}O_3$, and $DyCr_{0.7}Fe_{0.3}O_3$ samples are 140 K, 174 K, and 160 K, respectively. The ac magnetic measurements not only confirmed the Cr^{3+} ordering transitions in these samples (obtained using dc magnetic measurements), but also clearly showed the Ho^{3+} ordering at ~10 K in the present $HoCrO_3$ and $HoCr_{0.7}Fe_{0.3}O_3$ samples, which to our knowledge, is the first ac magnetic evidence of Ho^{3+} ordering in this system. The effective magnetic moments were determined to be $11.67\mu_B$, $11.30\mu_B$, and $11.27\mu_B$ for the $HoCrO_3$, $HoCr_{0.7}Fe_{0.3}O_3$, and $DyCr_{0.7}Fe_{0.3}O_3$ samples, respectively. For the first time, the magnetocaloric properties of $HoCrO_3$ and $HoCr_{0.7}Fe_{0.3}O_3$ were studied here, showing their potential for applications in magnetic refrigeration. In an applied dc magnetic field of 7 T, the maximum magnetocaloric value were determined to be 7.2 (at 20 K), 6.83 (at 20 K), 13.08 J/kg K (at 5 K) and the relative cooling power were 408, 387, and 500 J/kg for the $HoCrO_3$, $HoCr_{0.7}Fe_{0.3}O_3$, and $DyCr_{0.7}Fe_{0.3}O_3$ samples, respectively.

1. Introduction

Magnetocaloric effect (MCE) is a magneto-thermal phenomenon in which the temperature of a material changes when it is exposed to a changing magnetic field adiabatically.[1–5] MCE is the basis of magnetic refrigeration (MR), a technology promising to replace traditional gas compression refrigeration, because it is safer, more efficient, compact, and environmentally friendly.[2,6,7] A candidate for magnetic refrigerant should have large magnetic entropy change $\Delta S_M(T,H)$ and large relative cooling power (RCP).[8] It should be noted that the MCE values of a material are related to the magnetic moment of metal ions in the material and large MCE value is usually obtained around the magnetic ordering temperature of the metal ion.[8] Rare-earths, such as Gd, Ho, Tb, and Dy have large magnetic moments.[9] For the above mentioned reasons, MCE has been widely studied in Gd alloys for room temperature applications and MR technology based on those are becoming commercially available.[8] Additionally, the ordering temperature of rare-earth ions in oxides based on rare-earths is low (below 20 K),[10–13] and therefore they have been widely

*[*)]Author to whom correspondence should be addressed. Electronic mail: menka.jain@uconn.edu

studied for MR at low temperature (below 80 K), [10,14–17] which is an promising alternative approach for current low temperature cooling technology dominated by the expensive and nonrenewable liquid helium refrigeration. [15,18] Among the oxide materials, the magnetoelectric multiferroic (ME MF) rare-earth manganites $RMnO_3$ (R stands for rare-earth ions) have recently been investigated for their MCE properties. For example, at the magnetic field of 5 T, $TbMnO_3$ bulk powder was reported to have large RCP ~ 103 J/kg and MCE values ~6.75 J/kg K at 16 K. [14] From the report of Shao *et al.*, $HoMnO_3$ bulk powder showed large RCP ~ 312 J/kg and MCE values ~12.5 J/kg K at 16 K and a magnetic field of 7 T. [19]

Recently, another ME MF oxide system based on rare-earths, rare-earth chromite ($RCrO_3$), has been explored for its MCE properties and suitability for MR. For example, in $DyCrO_3$ (DCO), large MCE value of 8.4 J/kg K and relative cooling power of 217 J/kg at 15 K and 4 T was first reported, which was attributed to the low-temperature ordering of Dy^{3+} at ~ 2.16 K. [15,20] This renders DCO useful for MR in the temperature range from 5 K to 30 K. These $RCrO_3$ materials stabilize in orthorhombically distorted perovskite structure and the exchange coupling between the Cr^{3+} nearest neighbors is predominantly antiferromagnetic (G-type) and these ions order magnetically at a Néel temperature (T_N^{Cr}) from 113 to 140 K depending upon R-ion. [21] Additionally, $RCrO_3$ systems are of great interest as these exhibit spin-reorientation, rare-earth ordering, [22] metamagnetic transition, or temperature induced magnetization reversal in some cases at low temperatures (< 50K). [23,24] In a similar system– rare-earth ferrite, for example, $DyFeO_3$, the Dy^{3+} ordering has been reported to occur at 4.5 K, [17,25] and a giant entropy change at 5 K (around Dy^{3+} ordering) was reported to be 16.62 J/kg K under field change of 2 T. [10] Among the rare-earth ions, Ho^{3+} has the second highest magnetic moment after Dy^{3+} (10.4 μ_B for Ho^{3+} as compared to 10.6 μ_B for Dy^{3+}). [9] In $HoFeO_3$ bulk powder, Ho^{3+} ordering has been reported to occur at 3.3 K or at 6.5 K, [12,26] While in $HoFeO_3$ single crystal, Ho^{3+} ordering was reported at 4.1 K and a spin reorientation was reported ~50-60 K; so, large MCE value of 19.2 J/kg K was obtained at the Ho^{3+} ordering temperature. [27] Yin *et al.* reported Dy^{3+} ordering temperature at 14 K in $DyCr_{0.5}Fe_{0.5}O_3$ and the maximum MCE value was improved to 10.5 J/kg K at 5 K and 4 T. [16] From above discussion, it is clear that $HoCrO_3$ (HCO) is likely to obtain large MCE values in slightly higher temperature range than DCO due to slightly higher Ho^{3+} ordering temperature. Further, by Fe^{3+} substitution at the Cr-site, the ordering temperature of Ho^{3+} is expected to increase and correspondingly its MCE value may maximize at a higher temperature compared to that in pure HCO, rendering it applicable for magnetic refrigeration in slightly higher temperature range than those for DCO. As in $RMnO_3$ system, Cr-O-Cr bond angle in $RCrO_3$ system would play an important role in its magnetic properties (and hence MCE properties) that would be modified with either R-site or Cr-site substitutions. [28,29] Therefore, in order to understand the structure-property correlations, it is of great importance to utilize first-principle to calculate the lattice parameters of the stable structure and density of states (DOS) complementary to experimental work.

In the present work, the structural, magnetic (ac and dc), and MCE properties of the HCO, $HoCr_{0.7}Fe_{0.3}O_3$, and $DyCr_{0.7}Fe_{0.3}O_3$ bulk powder samples have been examined. In addition, the lattice distortions and density of states are studied using the first principle calculations based on density functional theory (DFT), which can provide crucial information that can lead to the design of materials with increased MCE properties. To our knowledge, this is the first work on the exploration of ac magnetic properties and MCE properties of HCO and Fe-substituted HCO. Also, RCP value of Fe substituted DCO is reported for the first time in addition to the density of state

calculations in the $RCrO_3$ system. Given that experimental study of such complex systems is not only time consuming and costly but also require sophisticated experimental techniques. A combined experimental and first-principles computational methods based study is capable to provide crucial insights about the physicochemical properties resultant form defects/impurities that complements experiments. To our knowledge, this is the first combined experimental and computational attempt to explore ac magnetic properties and MCE properties and electronic structure of HCO and Fe-substituted HCO, and potentially will enhance the efforts towards synthesis and design of new ME MF materials.

2. Experimental and computational details

The $HoCrO_3$ (HCO), $HoCr_{0.7}Fe_{0.3}O_3$ (HCFO), and $DyCr_{0.7}Fe_{0.3}O_3$ (DCFO) bulk powder samples were synthesized via citrate solution route. High-purity $Dy(NO_3)_3$, $Ho(NO_3)_3$, $Cr(NO_3)_3$, and $Fe(NO_3)_3$ precursors were first dissolved in water in stoichiometric ratio and then mixed together. After addition of citric acid, the solutions were heated and dried. The powder thus obtained was ground in a mortar and then annealed at 900 °C in oxygen for 2 hours. To determine the structure of the samples, the room-temperature X-ray diffraction (XRD) patterns were measured by Bruker D8 x-ray diffractometer using Cu-Kα radiation (λ=1.542 Å). The scan speed was 2° per minute with a step of 0.02° in the range of 20°<2θ<90°. Rietveld refinement was carried out with Fullprof Suite software. The purity of the samples were further confirmed by room temperature Raman scattering measurements using an Ar-ion laser (Renishaw System 2000) with a wavelength of 514 nm. The surface morphology of the powder samples were detected by field-emission scanning electron microscope (FESEM). The dc magnetic property was measured using the Vibrating Sample Magnetometer attached to the Evercool physical property measurement system (PPMS, from Quantum Design). For the magnetization vs. field (M vs. H) measurements, the samples were first zero field cooled to 5 K. The M vs. H data was measured with the field from 0 to 7 T and back to 7 T. The magnetic field was then set to 2 T and oscillated to back to zero field followed by increment of temperature by 5 K for the next M vs H measurements. This procedure was repeated until the sample temperature was above the Néel temperature of the material. The frequency dependence (100, 500, and 1000 Hz) of ac susceptibility were measured in the temperature range of 5-300 K using the ac susceptibility option attached to the PPMS.

In order to further understand the crystal and magnetic structure, DFT based spin-polarized first-principles calculations are performed using the projector augmented wave method as implemented in the Vienna *ab-initio* simulation package.[30–32] In present calculations, the exchange correlation interaction is treated within the generalized gradient approximation (GGA) using the Perdew-Burke-Ernzerhoff (PBE) functional.[33] The electronic wave functions were expanded in a plane wave basis with a cut off energy of 500 eV. It is noteworthy that due to the errors associated with the on-site Coulomb and exchange interactions,[34] DFT based methods are known to fail to reproduce an accurate description of the electronic structure for strongly correlated systems such as transition metal oxides[35–37] and rare-earth compounds.[28] In such cases, the accuracy of DFT can be improved by incorporating a Hubbard-model-type correction (U), which accounts for localized d and f orbitals. Hence, in the present work to describe the localized nature of the f states, in all the calculations U values ~ 3.7 eV and 3.9 eV are used for Ho and Dy, respectively.[28,38,39] A Monkhorst-Pack k-point mesh of 5×5×4 is employed to produce converged results within 0.1 meV per formula unit. In doped cases, one Cr atom was substituted with dopants Fe. It

should be mentioned that 25 at% was chosen for Fe concentration in DFT calculations not only to be close to experimental results but also to keep a reasonable super cell size. We expect the trend in physical properties of 25% doped samples to be similar as for 30 at% doped samples.

3. Results and discussion

Fig. 1(a), (c), and (d) show the XRD patterns and corresponding Rietveld refinements of the HCO, HCFO, and DCFO samples, respectively. The difference between the refinement model and experimental data (also plotted in Figure) is minimal, indicating that the samples are phase-pure and stabilize in a distorted orthorhombic perovskite with the space group *Pbnm*, as shown schematically in Fig. 1(b). The Fig. 1(b) shows the corner shared CrO_6 octahedra and the Cr ions in the center of the octahedral. The DFT obtained XRD data is also plotted in the figure. The *a*, *b*, and *c* lattice parameters obtained from the Rietveld refinement model and the DFT (PBE+U) calculations are close to the reports of pure HCO and DCO [22,40,41] and in good agreement, as summarized in Table 1. The experimentally obtained *a*, *b*, and *c* lattice parameter values (The lattice parameters for HCFO were found to be larger than those of HCO, which can be explained by the difference in the ionic size of Fe^{3+} and Cr^{3+} (Table 2). In Fe doped samples, both Fe^{3+} and Cr^{3+} have a coordination number of 6. The magnetic moment (μ), ionic radii (*r*, from Shannon's ionic radii database)[42], and atomic mass (*u*) of Ho^{3+}, Dy^{3+}, Fe^{3+} and Cr^{3+} are summarized in Table 2. The ionic radii of Fe^{3+} is slightly larger (0.645Å, for high spin state) than that of Cr^{3+} (0.615 Å). Thus, substitution of slightly bigger ion (Fe^{3+}) in the lattice would account for the increased lattice parameters of HCFO as compared to HCO. Further, the lattice parameter of DCFO was slightly larger than that of HCFO because of the larger ionic radii of Dy^{3+} (1.083 Å) as compared to that of Ho^{3+} (1.072 Å).

Table 1. Lattice parameters obtained from DFT (PBE+U) and Rietveld refinement of the experimental XRD data (EXP) along with the crystallite size/strain calculated using Williamson-Hall analysis for $HoCrO_3$ (HCO), $HoCr_{0.7}Fe_{0.3}O_3$ (HCFO), and $DyCr_{0.7}Fe_{0.3}O_3$ (DCFO) samples.

Parameter		HCO	HCFO	DCFO
a (Å)	DFT (PBE+U)	5.269	5.247	5.229
	EXP	5.248	5.259	5.280
b (Å)	DFT (PBE+U)	5.543	5.600	5.5808
	EXP	5.525	5.540	5.536
c (Å)	DFT (PBE+U)	7.585	7.567	7.555
	EXP	7.545	7.564	7.577
V(Å^3)	DFT (PBE+U)	221.52	222.37	220.50
	EXP	218.79	220.40	221.48
Crystallite size (nm)		104.1±13.3	142.9 ± 26.1	119.1 ± 14.7
Strain		(6.8 ± 3.5)×10^{-4}	(17.0 ± 3.6) ×10^{-4}	(10.3 ± 3.3) ×10^{-4}

Table 2. The values of magnetic moment (μ), ionic radii (r), and atomic mass (m) of Ho^{3+}, Dy^{3+}, Fe^{3+}, and Cr^{3+} ions.

	Ho^{3+}	Dy^{3+}	Fe^{3+}	Cr^{3+} (spin only)	Ref.
μ (μ_B)	10.4	10.6	5.9	3.8	9
r (Å)	1.072	1.083	0.645	0.615	42
m (u)	164.9	162.5	55.85	52.00	43

The crystallite size and strain of the present powder samples were estimated using Williamson-Hall (W-H) analysis, expressed by the formula: [44]

$$\beta \cos \theta = C_\varepsilon \sin \theta + \frac{K\lambda}{L}, \tag{1}$$

where β is full width at half maximum (FWHM) of the diffraction peak, θ is the Bragg angle, C_ε is the strain, $K \approx 0.89$ is a constant, λ is the wavelength of the X-ray beam, and L is the crystallite size. From the XRD data, β was obtained by Pearson 7 peak fit using the Fityk software. The values of L and C_ε were then calculated and summarized in Table 1. The crystallite sizes of the present powder samples are around 90-170 nm, which are slightly bigger than those reported for GdCrO$_3$ nano particles (~50 nm) synthesized by hydrothermal method [45,46] and DCO nano-platelets (~50-90 nm) synthesized by hydrolytic sol-gel method. [41] It should be noted that the strain in the samples are much smaller than 1%, indicating that distribution of defects from the present synthesis route is minimal.[47] The uncertainty here is obtained from mean-squared-error (MSE) between the experimental data and model. The microstructures of the samples were examined by the FESEM as shown in Fig. 2. The images do not show any obvious presence of impurity and the particles appear to be of uniform sizes for all the present samples. It is clear from the figure that the average particle size of HCFO (Fig. 2 (a)) is slightly larger than those of HCO and DCFO (Fig. 2 (b) and (c)). This is in agreement with the result presented in Table 1 obtained from W-H analysis.

Complementary to XRD, Raman spectra provides useful data of the phonon spectra and structural distortion of RCrO$_3$.[48] The room temperature Raman spectra of the three samples are shown in Fig. 3. RCrO$_3$ with orthorhombic *Pbnm* structure possess 24 Raman active modes ($7A_g+5B_{1g}+7B_{2g}+5B_{3g}$).[16,48] In Fig. 3, the mode assignments were done following the work by McDannald *et al.* and Yin *et al.*[15,16] It should be noted that all the observed peaks in Raman spectra of the present samples could be assigned for the RCrO$_3$ system. Strong peaks at ~ 693 cm^{-1}, 676 cm^{-1}, and 676 cm^{-1} were observed for HCO, HCFO, and DCFO, respectively and were not reported in most cases for RCrO$_3$, which are attributed to the antisymmetric stretching of FeO$_6$ or CrO$_6$ octahedra in RCrO$_3$.[16] Raman peaks are sensitive to impurities and structure of the material. In the present samples, no extra peaks of impurities (such as Fe$_2$O$_3$, Cr$_2$O$_3$, or Fe$_3$O$_4$, etc) were observed in the Raman spectra. Thus, it is concluded that the present samples are phase pure, further corroborating the XRD results.

In order to investigate the interaction of orbital and magnetic ordering, we examine the electronic structure of the present samples by analyzing the density of states (DOS). Computed total and atom projected DOS of pure and doped HCO (or DCO) samples are plotted in Fig. 4,

where Fermi level is aligned to zero for convenience. As it can be seen in Figure 4(a) & (b), both pure HCO and pure DCO are found to be insulator with energy gap of about 3.1 eV and 2.7 eV, respectively. It should be noted that the DFT calculated band gap here is close to the recently reported experimentally obtained energy-gap values for HCO (3.26 eV)[49] and DCO (2.8 eV)[50]. The small difference between experimental and computed band-gap values is due to the well-known deficiency of conventional DFT methods in predicting band-gaps. Fig. 4 also clearly suggests that: (a) the valence band of the total DOS has contributions from both rare-earth and transition metal elements and (b) in the valence band the majority of the DOS in the vicinity of the Fermi-level, arises from the d-states of the Cr/Fe atoms. The notable point is that the in valence band highest occupied level shows O $2p$ character, while in conduction band the lowest unoccupied level has Cr $3d$ character. While the DOS in the conduction band can be explained in terms of optical conductivity spectra where the first peak mainly an attribute of the first optical transition as observed in the earlier optical conductivity spectra measurements.[50] Furthermore, in the conduction band the DOS have contributions from both Cr and O atoms but mainly dominated by Cr ($3d$) orbitals. On the other hand in Fe doped HCO/DCO, the DOS in the vicinity of the Fermi-level are largely contributed by Fe, which result into a shift in valence band maximum. This shift can be explained on the basis of the hybridization of d-orbitals of Fe and Cr with p-orbitals of oxygen in the valance band.[28] The O ($2p$) states and Cr/Fe ($3d$) states further enhance the strong hybridization between the orbital and spin order resulting in the magnetic and structural modulations, consistent with the Jahn-Teller mechanism.[28]

The temperature dependence of the dc magnetization (mass)with an applied magnetic field (H) of 50 Oe measured in both zero-field cooled (ZFC) and field cooled (FC) mode are exhibited in Fig. 5. The Néel temperature (Cr^{3+} ordering temperature, T_N^{Cr}) was observed at 140 K, 174 K and 160 K for HCO, HCFO and DCFO samples, respectively. As it can be seen that the T_N^{Cr} of HCFO and DCFO were higher than those of pure HCO and DCO, respectively [15], which is attributed to the effect of Fe substitution. It is worth noting that the present DCFO sample shows a lower T_N^{Cr} than 261 K reported recently for DyCr$_{0.5}$Fe$_{0.5}$O$_3$.[16] This indicates that the T_N^{Cr} is tunable in DyCr$_{1-x}$Fe$_x$O$_3$ (similarly for HoCr$_{1-x}$Fe$_x$O$_3$) solid solution by controlling the Cr^{3+}/Fe^{3+} ratio. In addition to the Néel temperature, another transition at 10 K was observed for DCFO, which can be attributed to the ordering of Dy^{3+}.[16] However, HCO or HCFO samples did not show the Ho^{3+} ordering in the temperature dependent dc magnetic data. The magnetization for the present HCO sample (max ~ 30 emu/g) is consistent with that reported by Tiwari et al. [40], but higher than the present HCFO sample (max ~21 emu/g). It should be noted that Shao et al. reported that in HoFeO$_3$ single crystal, the maximum magnetization value was ~4.5 emu/g at 100 Oe, which is much lower than that of HCO.[27] Thus, the reduction in magnetization of the present HCFO samples could be due to iron substitution. The magnetization of DCFO was in good agreement with the report of 50% Fe substituted DCO, the magnetic susceptibility of both are ~0.02 emu/(gOe) {calculated using $\chi = M/H$, where M is the magnetization (mass) and H is the applied magnetic field.[16] However, the maximum magnetization of the present DCFO is much smaller than those of HCFO or HCO samples, because of the ordering of Dy^{3+} ions (see Fig. 5(c)).

The dc susceptibility in the FC mode of the samples was fitted by the Curie-Weiss law (χ = $C/(T-\theta)$) in the paramagnetic region (above T_N^{Cr}), as shown in Fig. 6 (a-c). Curie constant (C)

and Weiss temperature (θ) were obtained for each sample and presented in Table 3. The effective magnetic moment (μ_{eff}) was then calculated from C values using [9]:

$$\mu_{eff} = \sqrt{\frac{3k_B C}{N}}, \tag{1}$$

where k_B is Boltzmann constant, N is Avogadro constant. The magnetic moment can be also calculated theoretically by using the free ionic moments:

$$\mu'_{eff} = \sqrt{\mu_R^2 + (1-x)\mu_{Cr}^2 + x\mu_{Fe}^2}, \tag{2}$$

where μ_R, μ_{Cr}, and μ_{Fe} are the free ionic moments of Ho^{3+}/Dy^{3+}, Cr^{3+}, and Fe^{3+} respectively, and x is the Fe substitution fraction. These results for all the present samples were also summarized in Table 3. The effective magnetic moment obtained from the Curie-Weiss fit and the values of μ'_{eff} as calculated above were found to be in good agreement with each other.

Table 3. The Néel temperature {T_N^{Cr} (K)}, the Weiss temperature θ (K), Curie constant C (emu K/(Oe mol)), and effective magnetic moment μ_{eff} (μ_B), obtained by Curie-Weiss fit of the dc susceptibility data. The value of μ'_{eff} is calculated by using free ionic moments (see Table 2 and equation 2).

Sample	HCO	HCFO	DCFO
T_N^{Cr} (K)	140	174	160
θ (K)	-36.47 $\pm$ 0.60	-15.31 $\pm$3.03	-25.71$\pm$ 2.12
C (emu K/(Oe mol))	17.01 $\pm$ 0.04	15.96$\pm$ 0.19	15.88$\pm$0.14
μ_{eff} (μ_B)	11.66 $\pm$ 0.01	11.30 $\pm$ 0.07	11.27$\pm$0.05
μ'_{eff} (μ_B)	11.23	11.35	11.44

The temperature dependent ac susceptibility data (real part χ', imaginary part χ'' in Fig. 7) was measured with an applied ac magnetic field of 10 Oe and frequencies between 100 and 1000 Hz. Both the $\chi'(T)$ and $\chi''(T)$ data revealed Cr^{3+} ordering temperatures at 140 K, 174 K, and 160 K, for HCO, HCFO, and DCFO, respectively corroborating the dc magnetic results presented above. In addition, an ordering temperature at ~ 10 K was observed for DCFO sample, indicative of the Dy^{3+} ordering as observed in the dc magnetic data. It should be noted that $\chi(T)$ data for HCFO (Fig. 7 (a) (b)) revealed anomaly ~ 10 K, which was not observed in dc magnetic data or $\chi''(T)$ data of the sample. This anomaly is indicative of Ho^{3+} ordering in the samples. To the best of our knowledge, the present data is the first ac magnetic data in literature showing ordering of the Ho^{3+} moments in pure or doped HCO.

In order to investigate the dependence of magnetic property on magnetic field, isothermal magnetization vs. magnetic field (M vs. H) curves were measured up to 4 T and 160 K, and representative data at 5 K, 50 K, 100 K, and 160 K are shown in Fig. 8. The magnetic behavior of all the samples changes from canted antiferromagnetic (AFM) in low temperature to paramagnetic at high temperature (above their respective T_N^{Cr}), which can be interpreted as the superposition of

three types of magnetic contributions: (i) the weak ferromagnetic contribution that can be attributed to the canting of the AFM order of the transition metals (Fe or Cr), (ii) the strong paramagnetic rare-earth sublattice, and (iii) pure AFM contribution from the transition metal (Dy or Ho) sublattice. From the isothermal *M-H* data of all the samples, the temperature dependence of the coercive magnetic field (H_c) and remnant magnetization (M_R) values were obtained and plotted in Fig. 9. As the temperature increases, the coercive field increases initially, and maintains at some level. Then it decreases slowly, and becomes zero at ~140 K, 160 K, and 170 K for HCO, HCFO, and DCFO near their T_N^{Cr} respectively. The H_c value of DCFO sample is much smaller than those of HCO and HCFO samples, indicating that DCFO has much smaller magnetic hysteresis. Comparatively, the M_R (Fig. 9(b)) decreases monotonically with increasing temperature and reaches zero at ~ 145 K for all the present samples. All of these features can be interpreted by the competition between the three aforementioned magnetic contributions. When the temperature is near T_N^{Cr}, the strong paramagnetic signal plays the dominant role in the magnetic behavior, so the samples show no magnetic hysteresis and both H_c and M_R are zero.

In order to further examine the figure of merit of these materials for the evaluation of their applications in MR, the present samples were also evaluated for their MCE behavior, which can be extracted from the isothermal *M-H* curves exhibited in Fig. 10 (measured up to 7 T field and only in first quadrant as mentioned in experimental section). The MCE properties can be characterized mainly by two factors: magnetic entropy change *ΔSM(T,H)* given by [8] :

$$\Delta S_M(T,H) = \int_0^H \left(\frac{\partial M(T,H)}{\partial T}\right)_H dH \approx \sum_i \frac{M_{i+1}(T_{i+1},H) - M_i(T_i,H)}{T_{i+1} - T_i} \Delta H \tag{3}$$

and relative cooling power (RCP) usually calculated by [8]:

$$RCP = |\Delta S_{max}| \times \Delta T_{FWHM}, \tag{4}$$

where *ΔTFWHM* is the full width at half maximum of the temperature dependent *ΔSM* data. Here we use the more accurate integration method to calculate RCP [20]:

$$RCP = -\int |\Delta S_{M,H}| dT \tag{5}$$

In Fig. 11, the MCE values (*ΔSM(T,H)*) were calculated and determined to be 7.2 J/kg K at 20 K for HCO, 6.83 J/kg K at 20 K for HCFO, and 13.08 J/kg K at 5 K for DCFO at maximum under the magnetic field of 7 T. The MCE values of HCO and HCFO are reported for the first time here and the maximum values were smaller than those of DCO andDCFO.[13,36] It is partly because larger magnetic hysteresis exists in HCO or HCFO than in DCO or DCFO (see Fig. 9), and thus more energy is lost in the thermal process, resulting in smaller MCE values. This is supported by the report of Phan *et al.*, in which they propose nearly zero magnetic hysteresis as a criteria to select material for magnetic refrigerant because of energy efficiency.[8] Also, the MCE value of HCFO (6.83 J/kg K) is slightly smaller than that of HCO (7.2 J/kg K), which indicates that Fe substitution decrease the MCE values in HCO. Conversely, the MCE value of DCFO (10.3 J/kg K), which is close to the report of DyCr$_{0.5}$Fe$_{0.5}$O$_3$ (10.5 J/kg K), [16] was larger than that of pure DCO (8.4 J/kg K) under the magnetic field of 4 T.[15] Therefore, it was inferred that Fe substitution

in DCO improves the MCE values. In Table 4, the MCE values, temperature (T_{max}) and magnetic field (H_{max}) where the maximum MCE values were obtained were summarized and compared to the references. T_{max} is ~ 20 K for both HCO and HCFO samples and ~5 K for DCFO sample. Such difference in the temperature of maximum ΔS_M value can be explained by the slightly higher ordering temperature of Ho^{3+} than that of Dy^{3+}, as presented in Fig 7. For HCO, another peak in ΔS_M value, though much weaker, was observed at 140 K. It was attributed to the ordering of Cr^{3+}, which has much smaller magnetic moment than Ho^{3+} (seen in Table 2). In Table 4, the MCE properties of the bulk samples were much smaller than $HoFeO_3$ and $DyFeO_3$ single crystals (19.2 and 16.62 J/kg K). Because the single crystals were shown to be direction dependent (as measured in other cases),[27] and the bulk samples show only the average effect and smaller MCE values.

RCP values of the present samples were calculated and plotted in Fig. 11(d), and also are compared with references at two different fields (4 T and 7 T) in Table 4. At 7 T, the RCP value of HCO sample (408 J/kg) is larger than those of the present HCFO (387 J/kg) and previously reported $HoMnO_3$ (312 J/kg),[19] but smaller than the present DCFO (500 J/kg). Further, at the lower magnetic field of 4 T, DCFO sample shows larger RCP value (258 J/kg) than that of previously reported DCO sample (217 J/kg).[15] It is worth noting that the RCP values of HCO, HCFO and DCFO generally follow the same trend as their ΔS_M (see Table 4), because RCP value is obtained by the integration of the ΔS_M over temperature (see Equation 5), and larger ΔS_M is more likely to result in larger RCP value. However, RCP also depends on the width of the ΔS_M versus temperature data and larger value of full width at half maximum is also more likely to result in larger RCP value. That explains why HCO bulk sample shows smaller entropy change than $HoMnO_3$ bulk sample and $HoFeO_3$ single crystal, but still larger RCP value (Table 4).

Interestingly, HCFO showed smaller MCE and RCP values than HCO, while DCFO showed larger MCE and RCP values than DCO, so the effect of Fe substitution on the MCE property of rare-earth chromites varies for different rare-earth ions. From Table 4, it is clear that HCO and HCFO samples show decent MCE and RCP values at slightly higher temperature (20 K) than that in DCO and $HoMnO_3$ (< 10 K). Thus, the HCO and HCFO samples are considered suitable for MR application in slightly higher temperature (~20 K).

Table 4. A comparison of the temperature (T_{max}) and magnetic field (H_{max}) where the maximum entropy change ($\Delta S_{M,max}$) and the relative cooling power (RCP) were obtained for some pure and Fe substituted rare-earth chromites, manganites, and single crystal ferrites.

Material	$\Delta S_{M,max}$ (J/kg K)	T_{max} (K)	H_{max} (T)	RCP (J/kg)	Reference
$DyCrO_3$	8.4	15	4	217	15
$DyCr_{0.5}Fe_{0.5}O_3$	10.5	5	4	-	16
$DyCr_{0.7}Fe_{0.3}O_3$	13.08	5	7	500	This work
	10.3	5	4	258	
$HoCrO_3$	7.2	20	7	408	
	4.2	20	4	189	
$HoCr_{0.7}Fe_{0.3}O_3$	6.83	20	7	387	
	3.74	15	4	167	

HoMnO$_3$	12.5	10	7	312	[19]
DyFeO$_3$ (single crystal)	16.62	5	2	150	[10]
	18.5	5	7	586	
HoFeO$_3$ (single crystal)	19.2	4.5	7	220	[27]

4. Conclusions

In summary, HoCrO$_3$ and Fe substituted HoCr$_{0.7}$Fe$_{0.3}$O$_3$ and DyCr$_{0.7}$Fe$_{0.3}$O$_3$ powder samples were prepared by a solution route. From x-ray diffraction data, the crystal structure were determined to be orthorhombically distorted perovskite structure (space group *Pbnm*) and the experimentally obtained lattice parameters were confirmed with those calculated using density function theory. The density of state calculations shows that band gap of DCO or HCO decreases with Fe doping. The dc magnetic measurement indicates the Cr^{3+} ordering temperature are at 140 K, 174 K, 160 K for HoCrO$_3$, HoCr$_{0.7}$Fe$_{0.3}$O$_3$, and DyCr$_{0.7}$Fe$_{0.3}$O$_3$ samples, respectively, which shows that Fe substitution increases the Cr^{3+} ordering temperature. The ac magnetic measurements for the first time reveal ordering temperature of Ho^{3+} moments at 10 K in HoCrO$_3$, and HoCr$_{0.7}$Fe$_{0.3}$O$_3$ samples. The isothermal magnetization data show the change of magnetic behavior from canted antiferromagnetic in low temperature to paramagnetic at high temperature. These features were interpreted by the temperature dependent coercive field and remnant magnetization. For the first time, the magnetocaloric properties of HoCrO$_3$ and HoCr$_{0.7}$Fe$_{0.3}$O$_3$ were studied, showing potential application for magnetic refrigeration. At 7 T field, the maximum change in entropy (ΔS_M) values were determined to be 7.2, 6.83, and 13.08 J/kg K for the HoCrO$_3$, HoCr$_{0.7}$Fe$_{0.3}$O$_3$, and DyCr$_{0.7}$Fe$_{0.3}$O$_3$ samples, respectively. The relative cooling power were found to be 408, 387, and 500 J/kg for the HoCrO$_3$, HoCr$_{0.7}$Fe$_{0.3}$O$_3$, and DyCr$_{0.7}$Fe$_{0.3}$O$_3$ samples, respectively.

Acknowledgments

References

1   V. K. Pecharsky, A. P. Holm, K. A. Gschneidner and R. Rink, *Phys. Rev. Lett.*, 2003, **91**, 197204.

2   K. A. GschneidnerJr, V. K. Pecharsky and A. O. Tsokol, *Reports Prog. Phys.*, 2005, **68**, 1479–1539.

3   N. S. Bingham, H. Wang, F. Qin, H. X. Peng, J. F. Sun, V. Franco, H. Srikanth and M. H. Phan, *Appl. Phys. Lett.*, 2012, **101**, 102407.

4   V. Franco, *Determination of the Magnetic Entropy Change from Magnetic Measurements : the Importance of the Measurement Protocol*, Sevilla, Spain, 2014.

5   V. Basso, C. P. Sasso, K. P. Skokov, O. Gutfleisch and V. V. Khovaylo, *Phys. Rev. B*, 2012, **85**, 014430.

6   T. Krenke, E. Duman, M. Acet, E. F. Wassermann, X. Moya, L. Mañosa and A. Planes, *Nat. Mater.*, 2005, **4**, 450–4.

7   S. Gama, A. Coelho, A. de Campos, A. Carvalho, F. Gandra, P. von Ranke and N. de Oliveira, *Phys. Rev. Lett.*, 2004, **93**, 237202.

8   M. H. Phan and S. C. Yu, *J. Magn. Magn. Mater.*, 2007, **308**, 325–340.

9   J. M. D. Coey, *Magnetism and Magnetic Materials*, Cambridge University Press, Cambridge, 2009.

10   Y.-J. Ke, X.-Q. Zhang, H. Ge, Y. Ma and Z.-H. Cheng, *Chinese Phys. B*, 2015, **24**, 037501.

11   T. Yamaguchi and K. Tsushima, *Phys. Rev. B*, 1973, **8**, 5187–5198.

12   W. Koehler, E. Wollan and M. Wilkinson, *Phys. Rev.*, 1960, **118**, 58–70.

13   Subba Rao Gv and Rao Cnr, *Appl. Spectrosc.*, 1970, **24**, 436–444.

14   M. Staruch, L. Kuna, A. McDannald and M. Jain, *J. Magn. Magn. Mater.*, 2015, **377**, 117–120.

15   A. McDannald, L. Kuna and M. Jain, *J. Appl. Phys.*, 2013, **114**, 113904.

16   L. H. Yin, J. Yang, R. R. Zhang, J. M. Dai, W. H. Song and Y. P. Sun, *Appl. Phys. Lett.*, 2014, **104**, 032904.

17   R. L. White, *J. Appl. Phys.*, 1969, **40**, 1061.

18   D. W. Hoch, UNIVERSITY OF WISCONSIN-MADISON, 2004.

19   M. Shao, S. Cao, S. Yuan, J. Shang, B. Kang, B. Lu and J. Zhang, *Appl. Phys. Lett.*, 2012, **100**, 222404.

20   A. McDannald and M. Jain, *J. Appl. Phys.*, 2015, **118**, 043904.

21   J. R. Sahu, C. R. Serrao, N. Ray, U. V. Waghmare and C. N. R. Rao, *J. Mater. Chem.*, 2007, **17**, 42.

22   A. McDannald, L. Kuna, M. S. Seehra and M. Jain, *Phys. Rev. B*, 2015, **91**, 224415.

23   K. Yoshii, *J. Solid State Chem.*, 2001, **159**, 204–208.

24   Y. Su, J. Zhang, Z. Feng, L. Li, B. Li, Y. Zhou, Z. Chen and S. Cao, *J. Appl. Phys.*, 2010, **108**, 013905.

25   E. F. Bertaut and J. Mareschal, *J. Phys.*, 1968, **29**, 67–73.

26   A. Bhattacharjee, K. Saito and M. Sorai, *J. Phys. Chem. Solids*, 2002, **63**, 569–574.

27   M. Shao, S. Cao, Y. Wang, S. Yuan, B. Kang and J. Zhang, *Solid State Commun.*, 2012, **152**, 947–950.

28   V. Sharma, A. McDannald, M. Staruch, R. Ramprasad and M. Jain, *Appl. Phys. Lett.*, 2015, **107**, 012901.

29   T. Goto, T. Kimura, G. Lawes, A. P. Ramirez and Y. Tokura, *Phys. Rev. Lett.*, 2004, **92**, 257201.

30   G. Kresse and J. Furthmüller, *Comput. Mater. Sci.*, 1996, **6**, 15–50.

31   G. Kresse and J. Hafner, *Phys. Rev. B*, 1994, **49**, 14251–14269.

32   G. Kresse and J. Furthmüller, *Phys. Rev. B*, 1996, **54**, 11169–11186.

33   J. P. Perdew, K. Burke, M. Ernzerhof, D. of Physics and N. O. L. 70118 J. Quantum Theory Group Tulane University, *Phys. Rev. Lett.*, 1996, **77**, 3865–3868.

34   V. I. Anisimov, F. Aryasetiawan and A. I. Lichtenstein, *J. Phys. Condens. Matter*, 1997, **9**, 767–808.

35   A. Jain, G. Hautier, S. P. Ong, C. J. Moore, C. C. Fischer, K. A. Persson and G. Ceder, *Phys. Rev. B*, 2011, **84**, 045115.

36   M. Staruch, V. Sharma, C. Dela Cruz, R. Ramprasad and M. Jain, *J. Appl. Phys.*, 2014, **116**, 9–14.

37   C.-H. Kuo, I. M. Mosa, S. Thanneeru, V. Sharma, L. Zhang, S. Biswas, M. Aindow, S. Pamir Alpay, J. F. Rusling, S. L. Suib and J. He, *Chem. Commun.*, 2015, **51**, 5951–5954.

38   A. Jain, S. P. Ong, G. Hautier, W. Chen, W. D. Richards, S. Dacek, S. Cholia, D. Gunter, D. Skinner, G. Ceder and K. A. Persson, *APL Mater.*, 2013, **1**, 011002.

39   G. Hautier, C. C. Fischer, A. Jain, T. Mueller and G. Ceder, *Chem. Mater.*, 2010, **22**, 3762–3767.

40   B. Tiwari, M. K. Surendra and M. S. R. Rao, *J. Phys. Condens. Matter*, 2013, **25**, 216004.

41   P. Gupta, R. Bhargava, R. Das and P. Poddar, *RSC Adv.*, 2013, **3**, 26427.

42   B. Y. R. D. Shannon, M. H, N. H. Baur, O. H. Gibbs, M. Eu and V. Cu, *Acta Cryst.*, 1976, **32**, 751.

43   M. E. Wieser, *J. Phys. Chem. Ref. Data*, 2007, **36**, 485–496.

44   P. Dutta, M. S. Seehra, S. Thota and J. Kumar, *J. Phys. Condens. Matter*, 2008, **20**, 015218.

45   A. Jaiswal, R. Das, K. Vivekanand, T. Maity, P. M. Abraham, S. Adyanthaya and P. Poddar, *J. Appl. Phys.*, 2010, **107**, 013912.

46   A. Jaiswal, R. Das, S. Adyanthaya and P. Poddar, *J. Nanoparticle Res.*, 2010, **13**, 1019–1027.

47   A. Khorsand Zak, W. H. Abd. Majid, M. E. Abrishami and R. Yousefi, *Solid State Sci.*, 2011, **13**, 251–256.

48   M. C. Weber, J. Kreisel, P. A. Thomas, M. Newton, K. Sardar and R. I. Walton, *Phys. Rev. B*, 2012, **85**, 054303.

49   G. Kotnana and S. N. Jammalamadaka, *J. Appl. Phys.*, 2015, **118**, 1–7.

50   P. Gupta and P. Poddar, *RSC Adv.*, 2015, **5**, 10094–10101.

51   A. Midya, S. N. Das, P. Mandal, S. Pandya and V. Ganesan, *Phys. Rev. B - Condens. Matter Mater. Phys.*, 2011, **84**, 1–10.
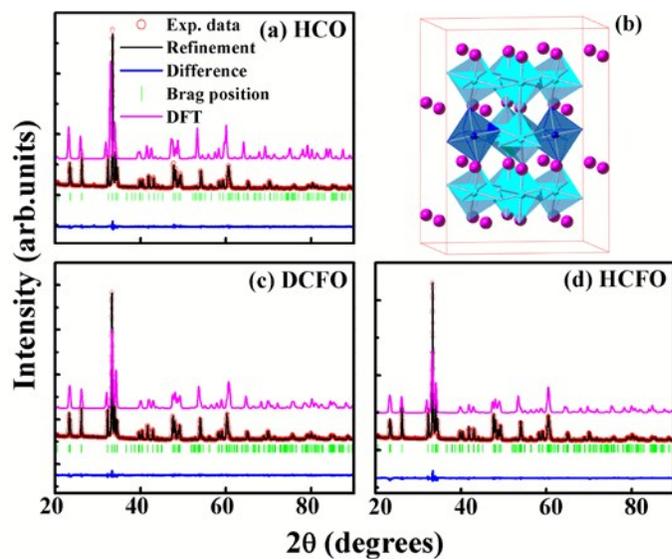
Fig. 1. The θ-2θ x-ray diffraction data (experimental and that obtained by DFT) and the Rietveld refinement of (a) holmium chromite (HCO), (c) 30% iron substitution holmium chromite (HCFO), and (d) 30% iron substitution dysprosium chromite (DCFO) samples. (b) Schematic of the crystal structure of perovskite $RCrO_3$ consists of CrO_6 octahedra where the Cr ions are in the center. Blue, pink, and cyan spheres stand for the Fe, Ho/Dy, and Cr atoms, respectively. The oxygen atoms are at the edge of octahedra and not shown here.
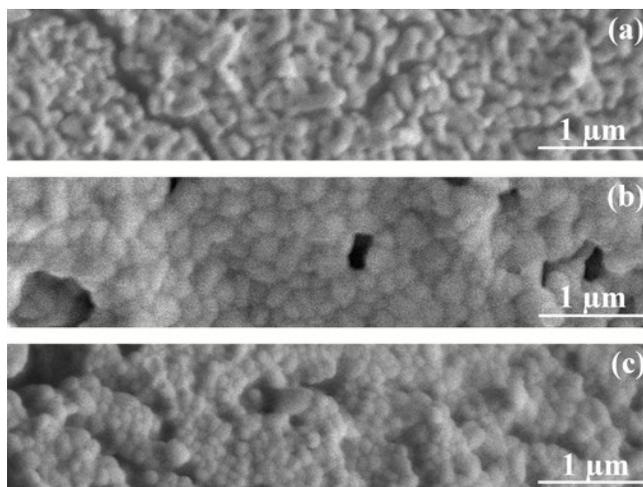
Fig. 2. Scanning electron microscopy images of the (a) holmium chromite (HCO), (b) 30% iron substitution holmium chromite (HCFO), and (c) 30% iron substitution dysprosium chromite (DCFO) samples.
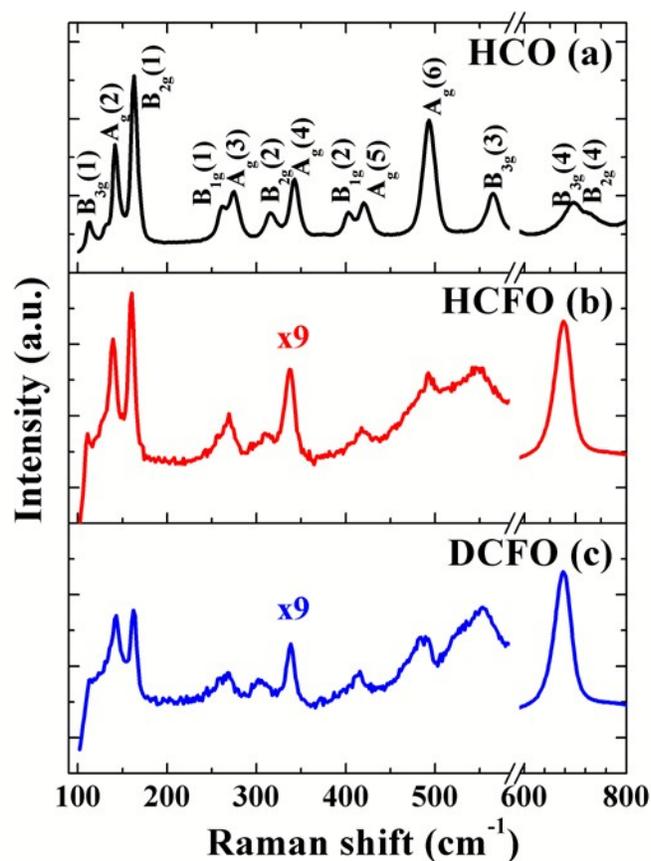
Fig. 3. Room temperature Raman spectra of (a) holmium chromite (HCO), (b) 30% iron substitution holmium chromite (HCFO), and (c) 30% iron substitution dysprosium chromite (DCFO) samples. There is a break from 584 to 590 cm^{-1}, because for (b), (c) the $B_{2g}(4)$ $B_{3g}(4)$ peak is much stronger than other peaks and the curve in the range of 100-584 cm^{-1} was amplified by nine times for clarity.
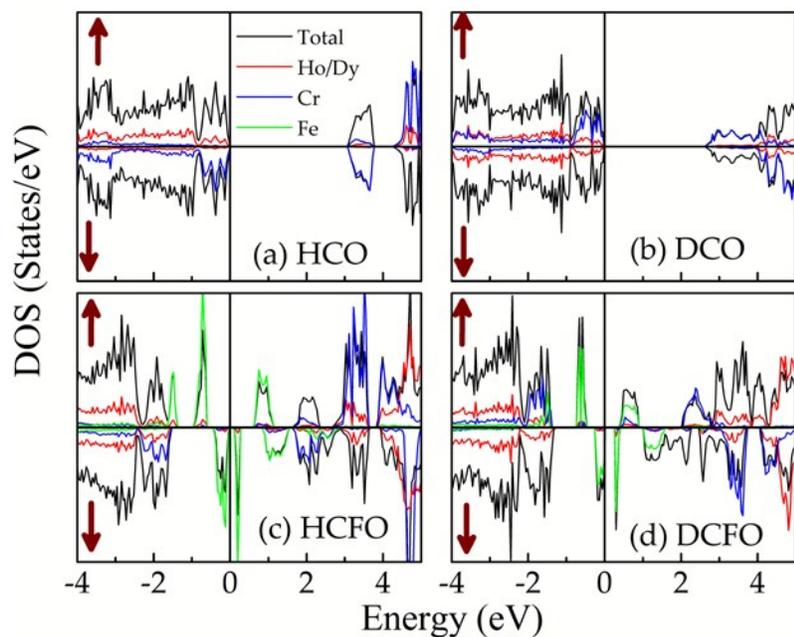
Fig. 4. Calculated total and atom projected DOS of (a) holmium chromite (HCO), (b) dysprosium chromite (DCO), (c) 30% iron substitution holmium chromite (HCFO), and (d) 30% iron substitution dysprosium chromite (DCFO) samples. In each case, both up and down arrows represents the up and down spin contributions to the DOS, respectively. The Fermi level is aligned to zero here.
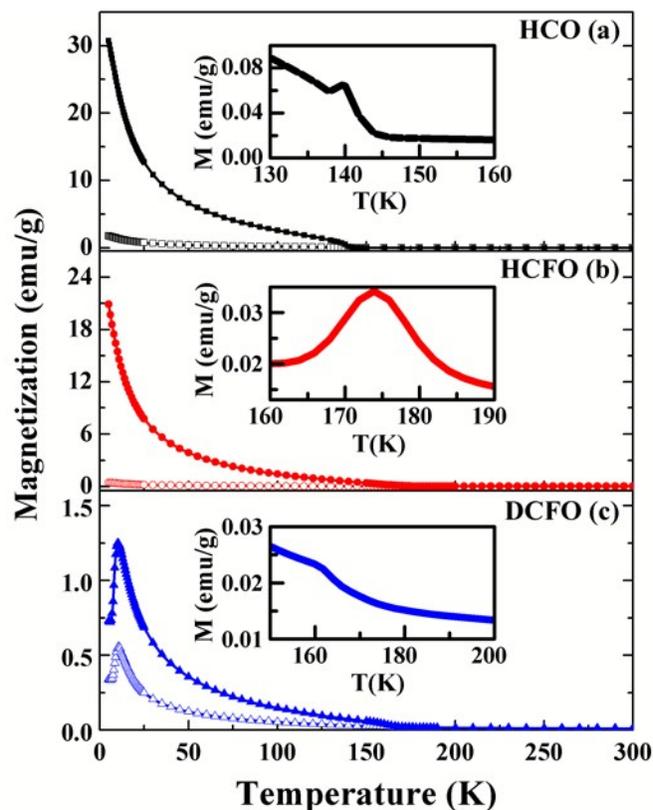
Fig. 5. The temperature dependent zero-field cooled (open symbols) and field cooled (closed symbols) dc magnetization (*M*) data of (a) holmium chromite (HCO), (b) 30% iron substitution holmium chromite (HCFO), and (c) 30% iron substitution dysprosium chromite (DCFO) samples measured at an applied field of 50 Oe.
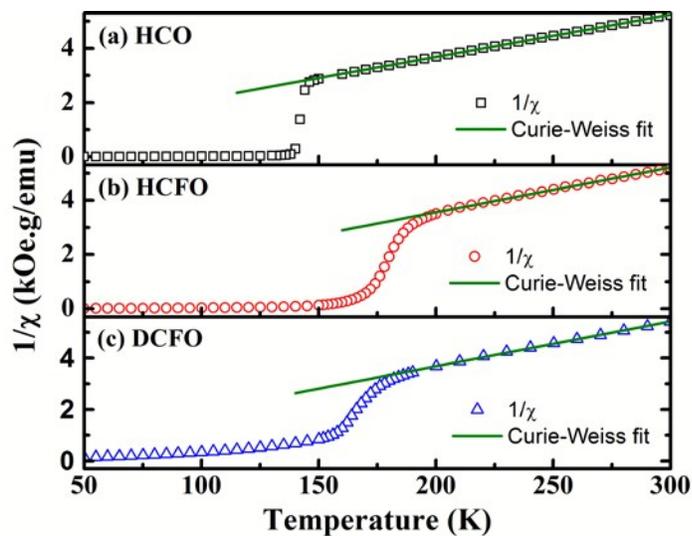
Fig. 6. The open circles show the inverse of the field-cooled dc susceptibility data as a function of temperature and the solid line shows the Curie-Weiss fit to the paramagnetic data of (a) holmium chromite (HCO), (b) 30% iron substitution holmium chromite (HCFO), and (c) 30% iron substitution dysprosium chromite (DCFO) samples.
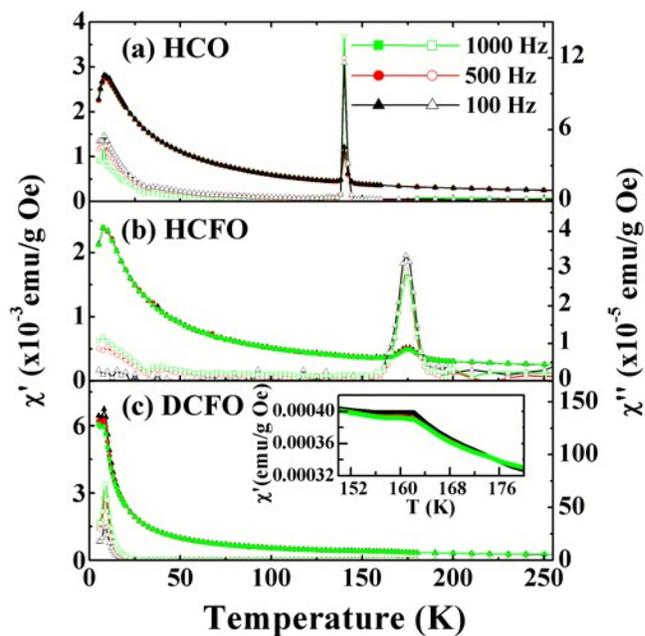
Fig. 7. The temperature dependent ac magnetic susceptibility data: real part χ' (closed symbols and left y-axis) and imaginary part χ'' (open symbols and right y-axis) of (a) holmium chromite (HCO), (b) 30% iron substitution holmium chromite (HCFO), and (c) 30% iron substitution dysprosium chromite (DCFO) samples measured at the 100 Hz, 500 Hz, and 1000 Hz. Inset of (c) shows the data in smaller temperature range for clarity.
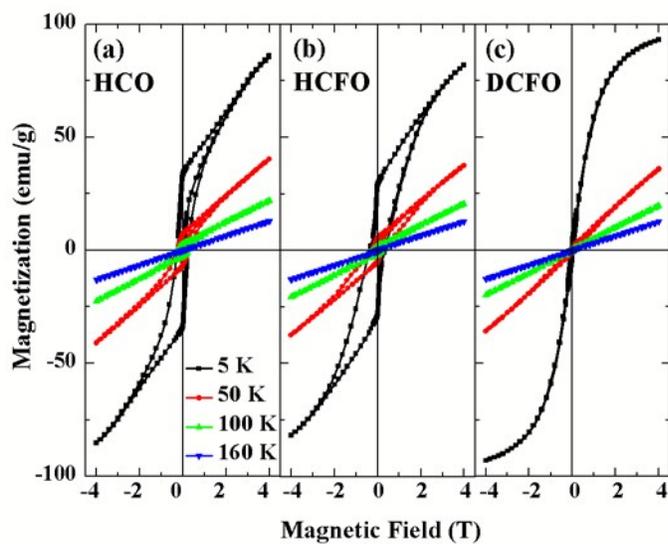
Fig. 8. Isothermal magnetization vs magnetic field data at 5 K, 50 K, 100 K, and 160 K for (a) holmium chromite (HCO), (b) 30% iron substitution holmium chromite (HCFO), and (c) 30% iron substitution dysprosium chromite (DCFO) samples.
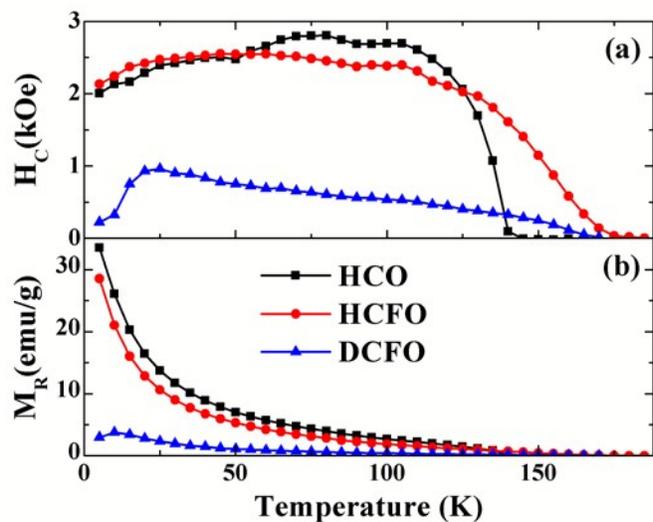
Fig. 9. The temperature dependent (a) coercive field (H_C) and (b) remnant magnetic moment (M_R) of holmium chromite (HCO), 30% iron substitution holmium chromite (HCFO), and 30% iron substitution dysprosium chromite (DCFO) samples.
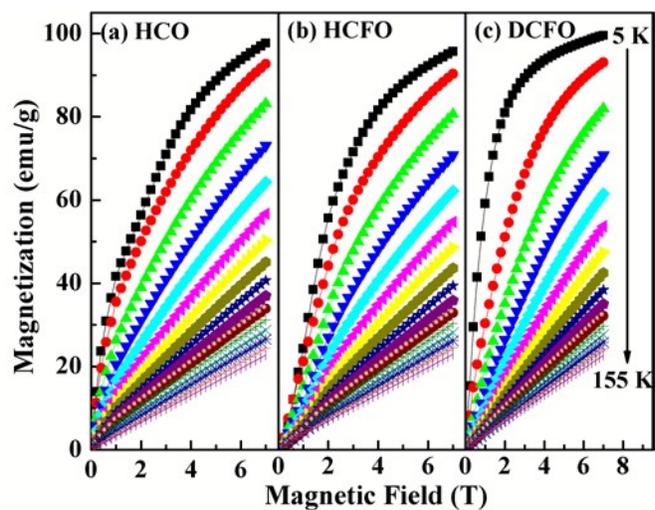
Fig. 10. Isothermal magnetization curves (in first quadrant) at many temperatures (5-155K) for (a) holmium chromite (HCO), (b) 30% iron substitution holmium chromite (HCFO), and (c) 30% iron substitution dysprosium chromite (DCFO) samples.

.
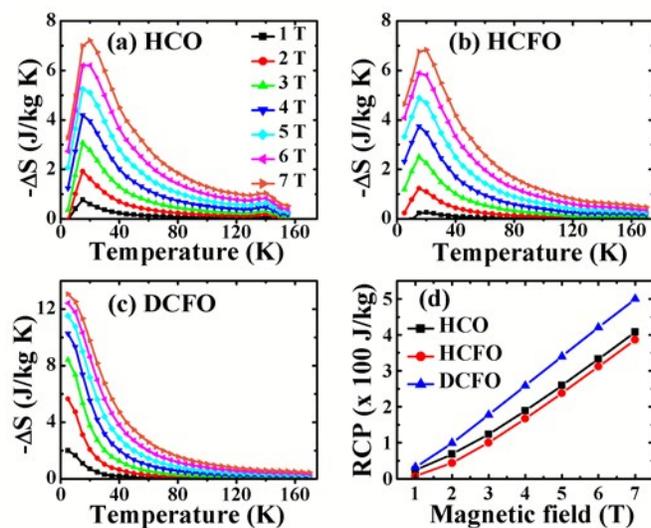
Fig. 11. The temperature dependent entropy change (ΔS) in (a) holmium chromite (HCO), (b) 30% iron substitution holmium chromite (HCFO), and (c) 30% iron substitution dysprosium chromite (DCFO) samples. The field dependent relative cooling power (RCP) values of the three samples are also presented in (d).

RSC Advances Accepted Manuscript

HoCrO$_3$ and DyCrO$_3$ powders were doped with Fe (HoCr$_{0.7}$Fe$_{0.3}$O$_3$ and DyCr$_{0.7}$Fe$_{0.3}$O$_3$) and the magnetocaloric properties were studied with the relative cooling power (RCP) values of 408, 387, and 500 J/kg at 7 T for the HoCrO$_3$, HoCr$_{0.7}$Fe$_{0.3}$O$_3$, and DyCr$_{0.7}$Fe$_{0.3}$O$_3$ samples, respectively, indicating their potential for applications in magnetic refrigeration.